The evolution of pellet size and shape during spheronisation of an extruded microcrystalline cellulose paste

C.L.S. Lau, Q. Yu, V.Y. Lister, S.L. Rough, D.I. Wilson* & M. Zhang[†]

Department of Chemical Engineering and Biotechnology, New Museums Site, Pembroke Street, Cambridge, CB2 3RA, UK

[†] School of Pharmacy, Health Science Center, Xi'an Jiaotong University, 76 Yanta Westroad, Xi'an Shannxi 710061, PR China

Chem Eng Res Des

Revised manuscript

December 2013

*Corresponding author

Dr D. Ian Wilson

Department of Chemical Engineering and Biotechnology
New Museums Site
Pembroke Street
Cambridge
CB2 3RA, UK

E-mail diw11@cam.ac.uk

Tel +44 1223 334791

FAX +44 1223 334796

The evolution of pellet size and shape during spheronisation of a microcrystalline cellulose paste

C.L.S. Lau, Q. Yu, V.Y. Lister, S.L. Rough, D.I. Wilson* & M. Zhang†

Department of Chemical Engineering and Biotechnology, New Museums Site, Pembroke Street, Cambridge, CB2 3RA, UK

†School of Pharmacy, Health Science Center, Xi'an Jiaotong University, 76 Yanta Westroad, Xi'an Shannxi 710061, PR China

Abstract

The process by which cylindrical rods of soft solid paste extrudate are converted into round pellets on a spheronsier (Marumeriser) plate was studied by interrupting spheronisation tests and measuring the size and shape of the pellets. Batches of 20 identical rods (20 mm long, 3 mm diameter) generated by ram extrusion of 47 wt% microcrystalline cellulose/water paste were spheronised at rotational speeds, ω, between 1200 rpm and 1800 rpm on a laboratory spheroniser. The time to complete spheronisation was found to scale with $\omega^{-3.6}$, which was close to the ω^{-3}dependency predicted by a simple collision model. Breakage occupied the first 10% of the process duration: rounding off was the rate determining step. The evolution of pellet shape was classified into five stages, the duration of which was found to scale with spheronisation time. Pellet shape, quantified by aspect ratio, circularity, shape and angularity factors presented by Sukumaran and Ashmawy (*Géotechnique*, 2001, Vol 51, 1-9), showed similar behaviour for all ω studied. A phenomenological model is proposed which identifies different routes for small and large rod breakage products.

Keywords: breakage, extrusion-spheronisation, microcrystalline cellulose, rounding, shape

1. Introduction

Extrusion-spheronisation (E-S) is widely used in the pharmaceutical and other industrial sectors for manufacturing dense pellets with high sphericity and density compared to other granulation methods (Haring *et al*., 2008). E-S is a two-stage process (Wilson and Rough, 2007): first, the particulate solids are combined with a liquid (the binder) to yield a dense suspension or paste which is extruded through dies or screens to give cylindrical extrudates; these extrudates are then spheronised (or *marumerised*) on a rotating friction plate to produce pellets. The term pellet is used here to differentiate the granule from the constituent particles.

E-S requires the material to exhibit plastic (or viscoplastic) behaviour so that the products (extrudates and pellets) retain their shape in the absence of deforming stresses or collisions. The stresses generated during extrusion give rise to extrudates with high density, which break down on the friction plate and are rounded by plastic collisions between pellets, and between the pellets and the wall. The collisions can also cause attrition, generating fines, which can attach to larger pellets (labelled 'mass transfer' by Koester *et al*., 2012). Several physical pathways are therefore involved in E-S, which make identification of suitable formulations for successful E-S challenging, as outlined by the reviews by Vervaet *et al*. (1995) and Wilson and Rough (2007). In particular, not only must the formulation be able to exhibit plastic behaviour for extrusion but it must also be able to be broken down and rounded off during spheronisation. The inclusion of microcrystalline cellulose (MCC) has been found to provide this behaviour and MCC is therefore widely used as an E-S aid (the 'gold standard' according to Koester and Thommes, 2013). Dukic-Ott *et al*. (2009) outlined some of the challenges involved in pharmaceutical pelletisation without using MCC as the excipient.

Formulation development can be improved by two different approaches. One is to use optimisation techniques to maximise the benefit of experimental trials, such as the response surface methodology reported by Desire *et al*. (2013). The second is to elucidate the physical mechanisms involved in E-S so that quantitative physical models can be constructed. These can then guide the interpretation of experimental data and, in due course, yield mechanistic tools which can be used to identify formulations *in silico*. The latter approach has been applied successfully in the fields of low- and high-shear granulation (see Salman *et al*., 2007; Vonk *et al*., 1997). This paper presents a short study of the fundamental steps involved in the spheronisation of MCC-water paste extrudates, and illustrates both the complexity of the

process and the steps that need to be investigated both independently and in parallel.

Conine and Hadley (1970) proposed that the basic criterion of successful spheronisation is that the extrudate must be able to break up into sections that are plastic enough to be rounded by the frictional forces on the rotating plate and collisions with pellets and walls. Figure 1 summarises the three phenomenological models for spheronisation in the literature.

Model A

Rowe (1985) reported that the cylindrical extrudates break into shorter lengths which collide with each other, the friction plate and the walls. The rods undergo plastic deformation which cause them to become rounded cylinders: these are subsequently rounded to a dumb-bell, then to an ellipsoid or egg-shape and finally a sphere.

Model B

Baert *et al*. (1993) suggested that rods are rounded by collisions with the walls and other pellets and become twisted, eventually breaking into sub-pellets with rounded and fractured sides. The latter faces are folded together by the rotating and frictional forces on the friction plate to form the near-spherical pellet. This folding action was claimed to explain why some pellets contain a cavity.

Model C

Liew *et al*. (2007) studied the effect of extrusion on E-S and observed in their spheronisation tests that pellets pass through the dumb-bell stage and become spherical by agglomeration of fines in the mid-plane or ‘waist’ region of the pellet. Koester *et al.* (2012) also advocated this model, in which attrition generates fines which subsequently re-attach to larger pellets in an agglomeration step. The tendency to form fines is determined by the friability of the material and the operating conditions.

All three models emphasise the role played by collisions between pellets and between pellets and the spheroniser surfaces. Measurement of the distribution of pellet positions and pellet velocities have become accessible using modern instrumentation techniques. Bouffard and co-workers (2012, 2013) have shown that pellet trajectories can be tracked and modelled in pan granulation systems, which are closely related to pharmaceutical spheronisers. Koester and

Thommes (2013) used particle image velocimetry (PIV) techniques to measure pellet velocities and flow patterns in a spheroniser. They reported that the pellet velocities were around one tenth that of the plate rim speed, and depended on the liquid content (which determines the cohesion between particulate material in the bed) and loading. This information can be combined with simulations of pellet breakage and plastic deformation (such as those reported by Sinka (2011)) to construct quantitative physical models.

Information about factors determining the key steps in spheronisation, *i.e*. whether Model A, B or C applies, is needed to link pellet scale processes to bulk behaviour. To this end, this paper reports a study of the evolution of pellet size and shape for a greatly simplified model system containing a small number of pellets. Features can be identified at the local level in a deterministic fashion rather than being inferred by analysis of data sets involving a large number of pellets. Tests were conducted with a 47 wt% MCC/water paste which has been shown to extrude and spheronise readily. Zhang *et al*. (2013) reported a range of MCC/water ratios for ram extrusion/spheronisation for the material used here (Avicel PH101) of 45-50 wt% MCC: 47 wt% MCC was selected as near the middle of this range.

Spheronisation tests were performed with an initial charge of 20 identically shaped extrudates: tests were stopped at different times and the pellet size and shape distributions measured. These results provide a base case for comparison with other studies investigating the influence of formulation *etc*. A small number of pellets were subject to detailed microstructure investigation.

2. Materials and methods

2.1 Extrudate preparation

Microcrystalline cellulose (Avicel PH101, FMC Corporation, Ireland) was provided by MSD Devlab (Hoddesdon, UK). The MCC powder characteristics were reported previously by Zhang *et al*. (2011) as: moisture content ~ 3 wt%; solid density 1538 kg m^{-3} (Mascia, 2008); particle size ranging from 2 to 260 μm with a Sauter mean diameter of 49.1 μm; particle shape ranging from larger fibrous rods to smaller irregular cuboids.

47 wt% MCC/water pastes were prepared following the procedure reported by Zhang *et al*. (2011). Dry MCC powder and deionised water were mixed together using a planetary mixer

fitted with a 'K'-beater attachment (Kenwood Ltd, UK) at different speeds. After mixing the paste was stored in a sealed plastic sample bag at room temperature for at least 1 hour before extrusion.

Cylindrical extrudates were generated using a Zwick/Roell Z50 strain frame configured to operate as a ram extruder. A detailed description of the apparatus is given in Zhang *et al*. (2011). A ram fitted with a high density polyethylene tip forced paste from a stainless steel (316 SS) cylindrical barrel (i.d. 25 mm) through a 316 SS concentric square entry die (i.d. D = 3 mm, length 16 mm). A charge of about 90 g of paste was loaded into the barrel, pre-compacted to 1 MPa to consolidate the material, then extruded at a ram velocity of 1 mm s^{-1}. The mean extrusion pressure was 8 MPa and this protocol yielded long, smooth, cylindrical rods of diameter equal to D, *i.e.* 3 ±0.01 mm. All tests were performed at room temperature (20-25°C) and relative humidity normally between 28-55%. Lower humidity levels promoted evaporation and hardening of the paste, which affected spheronisation. Extrudates were covered with a sheet of 'cling film' until used in order to minimise water loss by evaporation.

2.2 Spheronisation

Spheronisation was performed using a Caleva Spheroniser 120 (Caleva Process Solutions Ltd., UK) fitted with a 119 mm diameter 316 SS cross-hatched friction plate (pyramidal elements on a square pattern, spacing 1.40 mm, height 0.86 mm and width at top 0.50 mm). Detailed spheronisation studies were performed at rotational speeds, ω, of 1200, 1400, 1600 and 1800 rpm, corresponding to plate rim velocities of 7.5-11.2 m s^{-1}. Higher speeds promoted noticeable water loss from the paste charge over the course of a test as a result of heat from the motor. Supplementary tests to establish the effect of ω on spheronisation end time were performed at 1100, 1250, 1500 and 1700 rpm.

Each spheronisation test employed a starting charge of 20 rods of length 20±0.5 mm cut fresh from the extruded material. The charge was weighed before and after each test to monitor mass loss due to fines, and the water content was checked after tests to determine any evaporative losses. Rods of equal length were used in order to track breakage: in industrial practice, the rod length in the feed is not controlled and interpretation of the breakage phase is therefore complicated by collisions between rods of different lengths from the outset. The spheroniser load was therefore relatively small, at approximately 4 g, but this meant that most

of the collisions that occurred involved fast moving pellets and the wall, friction plate or other pellets. The characteristic velocity can then be expected to scale with the plate rim speed and is not affected by bed composition and depth, which Koester and Thommes (2013) observed for larger charges using PIV techniques. Figure 2 and the supplementary video [supplementary material] shows that the pellets quickly migrated towards the outer rim of the plate and participated in collisions in this region, mirroring the toroidal behaviour observed with larger charges (see, for example, Koester and Thommes (2013)).

The time taken to complete spheronisation, t_{end}, at a given rotational speed was determined initially by trial and error, running a test until all the pellets were spherical or nearly spherical as judged by eye. This was checked by measuring the shape distribution of the pellets afterwards, as described below. The shape factors obtained indicated that the pellets had attained values close of those of a sphere by the time spheronisation was judged by eye to be complete. Tests were subsequently run for shorter times, halted, and the pellets removed for size and shape analysis. A fresh batch of rods was used for each stopping time, t_s. The stopping times were selected to give similar values of the dimensionless stopping time, $t^* = t_s/t_{end}$. Some tests were repeated in order to establish reproducibility: this was generally good, unless the relative humidity level was low as this resulted in pellets drying out, becoming harder and not rounding as readily.

2.3 Pellet characterisation

At the end of each spheronisation test the batch was weighed and all the pellets were gently sieved using a 2 mm mesh to remove any fines present, in order to simplify the pellet shape analysis. The pellets were placed on a black base and photographed using a digital camera. The images were analysed using ImageJ (National Institutes of Health, USA) and Matlab® (Mathworks, USA) in order to calculate the following parameters.

Aspect ratio, *AR*

This is defined as the ratio of the length of the minor and major axes, *b* and *l*, respectively, of a 2-D projection of the pellet:

$$AR = \frac{b}{l} \qquad [1]$$

The major axis is the longest chord, passing through the centroid of area, connecting two

points on the projection, while the minor axis is the chord normal to the major axis. The aspect ratio is of limited use in describing shape (Bouwman *et al*., 2004) but it provides a convenient measure for monitoring breakage of rods.

Circularity, *C*

This shape factor is calculated from

$$C = \frac{4\pi A}{P^2} \qquad [2]$$

where *A* is the projected area of the pellet and *P* its perimeter, both determined by image analysis. For a sphere, *C* = 1.

Shape and angularity factors, *SF* and *AF*

Dumb-bell shaped pellets cannot be reliably identified by 'roundness' measures such as *C*, equivalent diameter *etc*., so the shape and angularity factor analysis presented by Sukumaran and Ashmawy (2001) was employed. Figure 3 illustrates this two-dimensional method. A circle is drawn around the projection of the pellet (it does not have to touch the projection). This confining circle is divided into *n* equal segments (*n* = 8 in Figure 3: the calculations reported here used *n* = 40, *i.e*. a sampling interval, ϕ, of 9º). The pellet is discretised by the intersection of the outline of the pellet with the radii defining the circle, *i.e*. points D, E and F in Figure 3. This provides an approximation of the true shape of the pellet.

The discretised pellet is then compared with the discretised confining circle. The deviation from circular behaviour can be quantified by calculating the distortion angles, labelled α_i, in Figure 3. The distortion angle is the difference between pairs of chords for the circle and the pellet. As this depends on the local shape of the pellet they can take positive or negative values. The absolute values of the distortion angles are summed and normalised by the sum of the distortion angles for an ellipse with a very small *AR* value (approaching a line) with the same number of intervals to give the shape factor, *SF*:

$$SF = \frac{4}{\pi}\frac{1}{n}\sum_{i=1}^{n}\left|\alpha_i\right| \times 100\% \qquad [3]$$

The internal angles, β_i, on the discretised pellet give a measure of the pellet angularity which can be defined quantitatively using the number and sharpness of the corners of the pellet. The angularity factor, *AF*, is then calculated using the following relationship which is normalised such that *AF* for a sphere is zero and *AF* of a cross or a four-pointed star is 100%:

$$AF = \frac{\sum_{i-1}^{n}(\beta_i - \pi)^2 - (4\pi^2/n)}{3\pi^2 - (4\pi^2/n)} \times 100\% \quad [4]$$

Sukumaran and Ashmawy (2001) reported shape and angularity factors for typical geometric shapes. *SF* and *AF* for a circle were both zero, as expected, while a square gave *SF* and *AF* values of 50% and 31%, respectively. They also analysed a range of sand particles from 8 different sand sources and reported that *SF* varied from 30-51% and *AF* varied from 7-29%. They concluded that the technique was suitable for identifying subtle variations between similar sands. The technique could also identify the slight irregularities in spherical glass ballotini with measured *SF* and *AF* of 4% and 2%.

2.4 Microstructure analysis

The density and voids distribution of a selected set of pellets were studied using X-ray microtomography. The pellets were dried at 60ºC under 0.2 bar vacuum for 24 h and imaged using a Skyscan 1172F system (Bruker, Kontich, Belgium) with a 20-100 kV X-ray source. Data acquisition of the projections was performed over 180º with rotation increments of 0.25º. Reconstruction of the tomographic cross-sections was performed using NRecon 1.6.8 for a cone beam geometry, with an isotropic voxel resolution of 2.5 µm. A series of 2-D images are presented. 3-D reconstruction and porosity estimation were not performed for this study.

3. Results and Discussion

3.1 Spheronisation time

Figure 4 shows that t_{end} decreases with increasing angular velocity, ω, as reported by Vervaet *et al*. (1995). The plot shows the trend line obtained by fitting the data to a power law relationship by least squares regression (correlation coefficient R^2 = 0. 9732)

$$t_{end} = 4\times10^{1}3\ \omega^{-3.6} \quad [5]$$

This dependency on ω is similar to that predicted by the simple model for plastic collisions, $t_{end} \propto \omega^{-3}$, outlined in the Appendix. The model provides a physical explanation for the decrease in the time to complete spheronisation with friction plate rim velocity reported for scale up by Newton *et al*. (1995). The model does not, however, consider the effect of rotation speed on pellet properties. For example, Hellén *et al*. (1993) and Schmidt and Kleinebudde (1998) both reported that higher rotation speeds yielded higher pellet densities. Individual pellet densities were not measured in this work.

Tests were also performed at 800 and 1000 rpm but did not yield spheroidal pellets. The pellets did not progress past the ellipsoidal (egg-shaped) stage. One reason for this was that the long duration of these tests made the extrudates prone to evaporation losses which led to stiffening of the material.

3.2 Rod breakage

Figure 5 shows a series of photographs for tests performed for different times at ω = 1200 rpm, illustrating how the number and shape of pellets evolve over time. The rods first break into shorter rods and dumb-bells appear. As spheronisation proceeds, the number of dumb-bells decreases and ellipsoids (egg-shaped pellets) become dominant (after 88 s, t^* = 0.30). Rounding of the ellipsoids follows and takes a relatively large fraction of the spheronisation time (~66%). It should be noted that each photograph represents a separate experiment.

The dominant pellet shape was assessed visually and five stages of shape evolution were identified as I – rods; II – dumb-bells (early stage, with visible cap formation); III – dumb-bells (later stage, with caps approaching or closing); IV – egg-shape; and V – spherical (spheroidal). Whilst subjective, these classifications gave a simple categorisation scheme. The time over which each shape was dominant is recorded in Table 1 for the four spheronisation speeds studied in detail. The time at which rods and dumbbells were no longer seen is also reported. The dimensionless times, *i.e*. $t^* = t/t_{end}$, corresponding to the stage boundaries and the disappearance of rods and dumb-bells show markedly good agreement. There is some variation in values, resulting from the coarseness of the times assigned to terminate the test and the uncertainty in t_{end}.

The agreement between the four data sets when time is scaled in this manner is an important result and has not, to the authors' knowledge, been reported before. It is also evident in subsequent plots (*e.g.* Figures 7 and 10). This finding suggests that the collision model in the Appendix provides a rational basis for understanding spheronisation and supports the fundamental studies of plastic deformation described by Sinka (2010, 2011).

The fines generated by breakage during spheronisation are not shown on Figure 5. The amount of fines could not be measured accurately as some material was lost to the machine internals, falling in the gap between the friction plate and the wall, and evaporation resulted in some moisture loss to the environment. The total amount lost was measured by difference and the results for tests at ω = 1200, 1400 and 1800 rpm are presented in Figure 6. The data set for ω = 1600 rpm were subject to a calibration error and are not reported. The Figure shows a sharp initial step and increase for all three data sets up to $t^* \sim 0.15$, and a steady level up to $t^* \sim 0.70$. The early increase is consistent with the rod breakage and initial rounding stages evident in Figure 5 and t^* for rod disappearance in Table 1. The plateau behaviour suggests that further fines are not generated in the rounding stages. The ω = 1200 rpm data set show a steady increase rather than approaching a plateau and this could be due to evaporation at longer times. This aspect can be investigated further in future work.

Rod breakage to create smaller pellets was quantified by counting the number of pellets retained on the 2 mm mesh sieve, N_p. t^* is plotted on a logarithmic scale so that the initial changes can be seen more easily. Figure 7(*a*) shows the evolution of N_p over the course of spheronisation at the four speeds tested in detail. N_p changes rapidly initially and reaches a steady value by $t^* \sim 0.15$ for each speed, indicating that rounding, rather than breakage, is the rate controlling step in these spheronisation tests. The period from $0 < t^* < 0.15$ is also that when fines generation, inferred from the mass loss data in Figure 6, is greatest.

The fluctuation in N_p values at $t^* > 0.1$, sometimes decreasing then increasing again, is a result of each data point deriving from separate experiments. A small number of tests were repeated to gauge reproducibility and confirmed that the variation in N_p was a systematic feature of the (random) breakage process. The shape and size factors showed the same trends. Quantitative analysis of the variation for repeated tests was not performed owing to the

limited time available. There are noticeably more pellets at 1800 rpm, indicating that this higher speed promoted more break-up than at the lower speed.

Figure 7(*a*) also shows the evolution in pellet major axis length. The error bars indicate the range of l values (similarly for AR in Figure 7(*b*)). As rods break, dimension l changes while the diameter remains constant (with $b = D$). Similar behaviour is evident at all four speeds. l increases rapidly in the early stage from its initial value of 20 mm. By $t^* \sim 0.15$, the mean l value is around 5 mm, and rods of this shape ($l/b < 2$) are not expected to break by bending. This is consistent with the observed transition to dumb-bells indicated by the regime boundaries. The range of l values decreases noticeably with time, and is relatively narrow once the breakage phased has ended. At extended t^*, l approaches 4 mm at all four speeds.

Also plotted on Figure 7 are the stage boundaries marking the transition in dominant pellet shape given in Table 1. The N_p data sets vary randomly about a mean at $t^* > 0.1$, indicating that there is (*i*) no systematic pellet coalescence and (*ii*) little densification with this material under these conditions. Plots of the area per pellet, not reported, showed a decline in the stages I and II, consistent with breakage, and little change thereafter. This reflects the trends seen in the N_p and l data sets.

The evolution of pellet shape, as quantified by *AR*, is plotted in similar form in Figure 7(*b*). The *AR* values increase rapidly from the initial value of 0.15 in the period $0 < t^* < 0.1$ (stages I and II) to ~ 0.75, which is associated primarily with breakage. *AR* changes more slowly thereafter (stages III-V, rounding), approaching a final value of approximately 0.95. The Figure shows that mean *AR* values follow a common, linear trend when plotted against log t^*. A physical explanation of this feature is the subject of ongoing work. In the latter stages the range in the *AR* values, denoted by the error bars, decreases noticeably for all but the 1600 rpm tests (in which fines attached to the pellets increase the projected area).

3.3 Shape evolution

The development of rounded pellets over time at 1200 rpm evident from the photographs in Figure 5 is compared quantitatively via the histograms of aspect ratio and circularity in Figure 8. The *AR* and *C* values at each time step are grouped into bins of width 0.1 units. Similar histograms were obtained at other speeds. The histograms show that both *AR* and *C* increase with time from their starting values of 0.15 and 0.36, respectively, converging towards final

values near 0.9 in each case. The latter values indicate that the final pellets are spheroidal and suitable for capsule fitting, as described by Chopra *et al*. (2002). Detailed optimisation of the spheronisation step to obtain more spherical pellets, *e.g*. by adjusting the formulation, was not undertaken here as the focus was on understanding the spheronisation process and because the material does not contain any active ingredient.

The *AR* histogram (Figure 8(a)) shows that the rods initially break into unequal lengths as most of the *AR* values lie between 0.3-0.7 rather than the value corresponding to bisection (0.3). The range of the *AR* values grows rapidly in the early stages, confirming that the position of the break on the extrudate is random. The lower limit of the *AR* range increases with t^* as longer rods break. The evolution of *C* values in Figure 8(*b*), including the range, is similar to the *AR* histogram. The largest change in the mean values for both parameters occurred at $t^* < 0.15$, in stages I and II, confirming that rounding is the rate determining step.

The distribution of *AR* and *C* values at each time step remains unimodal but are not normally distributed. It is therefore not appropriate to use statistical measures based on the normal distribution for these small data sets. Similar behaviour was observed at the other speeds. These results suggest that breakage could be modelled using population balance techniques such as those developed for agglomeration processes (*e.g.* Hounslow *et al*., 2001) but the simultaneous evolution of particle shape after $t^* \sim 0.1$ constitutes an important mechanistic step that is not included in existing agglomeration models.

The evolution of pellet shape at ω =1200 rpm is presented as trajectories in *AR*-*C* space in Figure 9. Each datum represents an individual pellet and the symbol shape denotes the time step. Also shown on the plots are the boundaries between the different stages in shape evolution in Table 1: the *AR* and *C* co-ordinates correspond to the mean values of each parameter at the boundary t^* values in Table 1. This assignation is somewhat subjective, as there is always a range of pellet shapes at a given time, but it serves to monitor the general trend in shape evolution. Given that the stage II/III transition is reached by $t^* \sim 0.15$, these plots emphasise that the pellets move through the breakage phases quickly and spend most of the time in the spheroniser being rounded off.

The *AR*-*C* plots for all four speeds studied in detail exhibited the same trend, in that the data

lie to the left of a curved locus which is very similar to that expected for breakage of cylindrical rods into shorter cylinders.

Consider a rod of length l and diameter D:

$$A = D \times l \quad [6]$$

$$P = 2(l + D) \quad [7]$$

$$C = \frac{4\pi A}{P^2} = \frac{\pi D / l}{(1 + D/l)^2} = \pi \frac{AR}{(1 + AR)^2} \quad [8]$$

Equation [8] is plotted for AR values up to 0.75, which represents a short rod which is not expected to break into smaller rods. This relationship represents the breakage locus in AR-C space. For pellets with $AR < 0.6$, it provides a bound on the pellet shape. At higher AR values the C data straddle the locus, which is consistent with rounding.

The evolution of the angularity and shape factors for the pellets at all four speeds is plotted in Figure 10. The data sets for 1200, 1400 and 1800 rpm follow a common dependency on t^*. The 1600 rpm data sets have significantly larger mean values and wider ranges. This difference arises because these pellets were not sieved to remove fines bound loosely to the pellets before being photographed. Both *AF* and *SF* are sensitive to the surface roughness arising from attached fines, whereas *C* and *AR* are insensitive.

The sieved pellet data sets show an initial increase in *AF* and *SF* with time, reaching 0.20-0.30 until $t^* > 0.12$, after which both measures decrease and approach a value ~ 0.10. Given that the *AF* and *SF* values for spheres are both zero, this indicates that the rods break and pass through a phase of strongly non-ellipsoidal and non-spheroidal shape which corresponds to the early dumb-bell stage when dumb-bells with noticeable waists are generated. The *AF* and *SF* values both decrease as the waists are filled in, either by attachment of fines or closure of the waist by the capped ends meeting.

3.4 X-ray microstructure analysis

The X-ray microtomography images of cross-sections in Figure 11 indicate the presence of regions of inhomogeneity associated with voids and low density. Figure 11(*a*) shows the initial 2 cm rod of extrudate to consist of a homogeneous matrix, with no noticeable variation in microstructure. The rod-shaped pellet in Figure 11(*b*) shows the same homogeneous matrix in the cylindrical part and slightly more dense material at the rounded edges, corresponding to the material there being compacted during collisions.

By comparison, there is noticeably greater variation in density in the early stage dumb-bell in Figure 11(*c*). The density is lower at the centre and higher at the edges, which is attributed to the collisions affecting the surface regions. In the later stage dumb-bell in Figure 11(*d*) the end caps have almost met at the centre. There are some air pockets at the waist where the material has been folded over, while at the centre the material is dense, suggesting that repeated collisions have compacted the whole matrix. It is also possible that fines are collecting at the waist and being incorporated into the matrix by repeated collisions.

In both dumb-bell images the material at the waist has a similar or higher density than the bulk material elsewhere in the pellet. There is no evidence of a plane of weakness in this region caused by twisting, or likely to break as a result of twisting, which is the mechanism for spheroid formation in Model B. Twisting-induced breakage would be expected to increase the number of particles by splitting in regions II and III, which is not observed in the N_p-t^* data sets.

The spheroidal pellet in Figure11(*e*) has a noticeably lower density at its centre than at the surface. This suggests that this pellet did not pass thorough the dumb-bell stage, which Figures 11(*c*) and (*d*) show to give high core densities. It is postulated that this pellet was generated by the uneven breakage of a longer rod to give a shorter segment, for which collisions result in rounding directly to spheroids. Comparison of the pellet sizes, and geometrical considerations of a plastic collision, suggest that the direct rounding mechanism would be expected for pellets with $l/D \leq 1.5$. This could be confirmed by further microtomographic analysis of more small pellets.

3.5 Spheronisation mechanism

The approach taken here, of starting with a set of identical rods, has allowed the mechanistic steps to be elucidated. There was no evidence supporting the rod twisting mechanism, Model B, in these experiments. Twisting could arise in larger beds of moving particles and this could be investigated using larger batch sizes. Twisting could also be absent because the paste, being stiff, is prone to breakage rather than twisting: tests with different paste rheology would be needed to explore this further. Rod breakage is a key step as it dictates the size of the sub-rods: if these are larger, they can undergo further breakage and/or form dumb-bells, while it is postulated that small sub-rods can be rounded directly into spheres.

Figure 12 is a schematic of this phenomenological model, which combines Model A and Model C. Breakage and rounding gives spheroidal pellets directly for smaller rod fragments, while longer rod fragments are postulated to go through a dumb-bell stage. Fines can attach at the waist of the dumb-bells: the contribution from fines will be determined by the tendency to form fines during breakage, which is linked to the rheology of the paste and the speeds reached in the spheroniser.

This model is now compared with the results reported for a similar MCC-water paste by Rough and Wilson (2005). They studied the spheronisation of extrudates with gross circumferential fractures generated by extrusion through short dies at high speed. The fractures were regular and were spaced a distance $D/2$ apart, which was expected to promote breakage into sub-rods of length $D/2$. Their spheronised pellets had a narrow size distribution centred on a mean diameter close to $D(3/4)^{1/3}$, which is the value expected for the volume of a pellet starting as a disc of diameter D and height $D/2$. In the current study rods did not break after they reached a length of 4-5 mm, *i.e.* $1.5D$. Smaller pellets with volume corresponding to rods shorter than this length are therefore postulated to have arisen from uneven breakage of long rods to give shorter fragments. The gross circumferential fracture observed by Rough and Wilson is beneficial for obtaining a narrow size distribution of smaller round pellets.

4. Conclusions

The mechanism by which rod-shaped extrudates transform into spheroidal pellets has been studied by monitoring the change of pellet dimensions and shape over the course of a spheronisation operation. The results indicate that the same mechanisms operate over the range of spheroniser rotational velocities studied here, except where drying promotes hardening of the paste over the course of the experiment.

Evolution of pellet shape was classified into five stages. The time spent in each stage was found to scale with the length of time to complete spheronisation across the range of rotational speeds, ω, studied. The time to complete spheronisation depended on $\omega^{-3.6}$, which is close to the dependency given by a simple collision model.

Rod breakage is a relatively fast process: rounding off proved to be the rate determining step. Whereas short rods tended to be rounded directly to spheroids, long rods tended to pass through a dumb-bell stage, in which fines can play an important role.

Acknowledgements

The X-ray microtomography experiments and analysis were performed by Dr Axel Zeitler. Assistance with the extrusion experiments from Matthew Bryan is also gratefully acknowledged. Microcrystalline cellulose for this final year student research project was kindly provided by MSD Devlab, Hoddesdon, UK.

Appendix – A simple model relating t_{end} and rotational speed

Figure 4 shows that t_{end} decreases with increasing ω. The following analysis provides a physical explanation for this trend.

During a collision the pellets are assumed to dissipate all their kinetic energy undergoing plastic deformation. The kinetic energy of the pellet is proportional to $\frac{1}{2}mV^2$, where m is the mass of the pellet and the maximum velocity, V, is related to the rotational speed and friction plate radius by $V = R\,\omega$.

The deformation work done per collision, E_d, is then given by

$$E_d = \tfrac{1}{2} mR^2\omega^2 \qquad \text{[A.1]}$$

Assuming that the rate at which pellets collide with the spheroniser walls is analogous to the rate of particle collisions in the perfect gas model, *i.e.* the collision rate $\propto V$, then the number of collisions in time t is proportional to $R\omega\, t$. If spheronisation requires a certain amount of plastic work per unit mass, W, resulting from N_c collisions, then

$$\begin{aligned} W \times m &= N_c \times E_d \\ &\propto \left(R\omega \cdot t_{end}\right)\tfrac{1}{2} mR^2\omega^2 \\ &\propto mR^3\omega^3 t_{end} \end{aligned} \qquad \text{[A.2]}$$

[A.2] indicates that

$$\omega^3 t_{end} = \text{constant} \qquad \text{[A.3]}$$

Nomenclature

Roman

A	Projected area	m^2
AF	Angularity factor	-
AR	Aspect ratio	-
b	Minor axis length	m
C	Circularity	-
D	Die diameter	m
E_d	Deformation work per collision	J
l	Major axis length	m
m	Mass of pellet	kg
N_p	Number of pellets	-
n	Number of segments	-
N_c	Number of collisions	-
P	Perimeter	m
R	Friction plate radius	m
R^2	Correlation coefficient	-
SF	Shape factor	-
t	Time	s
t_s	Time at which test is stopped	s
t_{end}	Time to complete spheronisation	s
t^*	Dimensionless time, $t^* = t_s/t_{end}$	-
V	Velocity of friction plate rim	$m\ s^{-1}$
W	Plastic work per unit mass	$J\ kg^{-1}$

Greek

α	Distortion angle, Figure 3	-
β	Internal angle, Figure 3	-
ϕ	Shape analysis sampling interval, Figure 3	-
ω	Spheroniser rotational speed	s^{-1}

References

Baert, L., Vermeersch, H., Remon, J.P., Smeyers-Verbeke, J. and Massart, D.L., (1993) Study of parameters important in the spheronisation process. *Int. J. Pharm.* ***96****, 225–229.*

Bouffard, J., Cabana, A., J. Chaouki, J. and Bertrand, F. (2012) Experimental investigation of the effect of particle cohesion on the flow dynamics in a spheronizer, *AIChEJ*, **59**(5), 1491–1501.

Bouffard, J., Bertrand, F., Chaouki, J. and Dumont, H. (2013) Discrete element investigation of flow patterns and segregation in a spheronizer. *Computers and Chemical Engineering*, **49**, 170–182.

Bouwman, A.M., Bosma, J.C., Vonk, P., Wesselink, J.A. and Frijlink, H.W. (2004) Which shape factor(s) best describe granules?, *Powder Tech*., **146**, 66-72

Conine J.W. and Hadley H.R. (1970) Preparation of small solid pharmaceutical spheres. *Drug Cosm. Ind.*, **106**, 38.

Chopra, R., Podczeck, F., Newton, J. M. and Alderborn, G. (2002) The influence of pellet shape and film coating on the filling of pellets into hard shell capsules, *Eur. J. Pharm. Biopharm.*, **53**, 327-333.

Desire, A., Paillard, B., Bougaret, J., Baron, M. and Couarraze, G. (2013) Extruder scale-up assessment in the process of extrusion-spheronization: comparison of radial and axial systems by a design of experiments approach, *Drug Dev. Ind. Pharm*., 39(2), 176-185.

Dukic-Ott, A., Thommes, M., Remon, J. P., Kleinebudde, P. and Vervaet, C. (2009) Production of pellets via extrusion-spheronisation without the incorporation of microcrystalline cellulose: A critical review, *Eur. J. Pharm. Biopharm.*, **71**(1), 38-46.

Haring, A., Vetchy, D., Janovska, L., Krejcova, K. and Rabiskova, M. (2008) Differences in characteristics of pellets prepared by different pelletization methods, *Drug Dev. Ind. Pharm*., 34(3), 289-296.

Hellén, L., Yliruusi, J., Merkku, P. Kristoffersson, E. (1993) Process variables of instant granulator and spheroniser: I. Physical properties of granules, extrudate and pellets, *Int. J. Pharm*., **96**, 197–204.

Hounslow M.J., Pearson J.M.K and Instone T. (2001) Tracer studies of high-shear granulation: II. Population balance modelling. *AIChE Jounal,* **47**(9), 1984-1999.

Koester, M. and Thommes, K. (2013) Analysis of particle kinematics in spheronisation via particle image velicometry, *Eur. J. Pharmaceutics Biopharmaceutics*, **83**, 307-314.

Koester, M., Willemsen, E., Krueger, C. and Thommes, M. (2012) Systematic evaluations regarding interparticular mass transfer in spheronisation, *Intl. J. Pharm.*, **431**(1-2), 84-89.

Liew, C.V., Chua, S.M. and Heng, P.W.S. (2007) Elucidation of spheroid formation with and without the extrusion step, *AAPS PharmSciTech*, **8**, 1-10.

Mascia, S. (2008) PhD Dissertation, University of Cambridge.

Newton, J.M., Chapman, S.R. and Rowe, R.C. (1995) The assessment of the scale-up performance of the extrusion/spheronisation process, *Int. J. Pharm*., **120**, 95–99.

Rough S.L. and Wilson D.I. (2005) Extrudate fracture and spheronisation of microcrystalline cellulose pastes. *Journal of Materials Science,* **40**, 4199-4219.

598 Rowe, R.C. (1985) Spheronization: a novel pill-making process? *Pharm. Int.*, **6**, 119–123.

599 Salman, A.D., Hounslow, M.J. and Seville, J.P.K. (eds.) (2007) *Granulation*, publ Elsevier,
600 Amsterdam.

601 Schmidt, C. and Kleinebudde, P. (1998) Comparison between a twin-screw extruder and a
602 rotary ring die press. Part II: influence of process variables, *Eur. J. Pharm. Biopharm*.
603 **45**, 173–179.

604 Sinka C.I. (2010) General framework for modelling the deformation of a body subject to a
605 large number of random impacts during spheronisation. *5th International Granulation*
606 *Workshop, University of Sheffield.*

607 Sinka, C.I. (2011) A first order numerical study of the spheronisation process, *Powder Tech*.,
608 206, 195-200.

609 Sukumaran B. and Ashmawy A. K. (2001) Quantitative characterisation of the geometry of
610 discrete particles. *Géotechnique, **51***, 1-9.

611 Vervaet S., Baert L., Remon J.P. (1995) Extrusion-spheronisation: A literature review. *Int J*
612 *Pharm*., **116**, 131-146.

613 Vonk, P., Guillaume, C.P.F, Ramaker, J.S., Vromans, H. and Kossen, N.W.F. (1997) Growth
614 mechanisms of high-shear pelletisation, *Intl. J. Pharm.*, **157**(1), 93-102.

615 Wilson, D.I. and Rough, S.L. (2007) Extrusion-Spheronisation, in *Granulation*, eds. Salman,
616 A.D. and Hounslow, M.J., publ Elsevier, Amsterdam, 189-210.

617 Zhang, M., Rough, S. L., Ward, R., Seiler, C. and Wilson, D. I. (2011) A comparison of ram
618 extrusion by single-holed and multi-holed dies for extrusion-spheronisation of
619 microcrystalline-based pastes. *Int. J. Pharm*., **416**, 210-222.

620 Zhang, M., Wilson, D.I., Ward, R., Seiler, C. and Rough, S.L.(2013) A comparison of screen
621 and ram extrusion-spheronisation of simple pharmaceutical pastes based on
622 microcrystalline cellulose, *Intl. J. Pharm*., **456**, 489-498

623

Tables:

Table 1 Absolute and normalised time boundaries of the stages in shape evolution at different spheroniser rotation speeds

Stage	Timing, t, s				Timing, normalised, t^*, -				t^*
ω /rpm	1200	1400	1600	1800	1200	1400	1600	1800	average
t_{end}	264	151	90	71	-	-	-	-	-
I Rod-shape	0-9	0-7	0-4	0-4	0-0.03	0-0.05	0-0.04	0-0.06	0-0.045
II Dumb-bell, early stage	9-18	7-12	4-10	4-7	0.03-0.07	0.05-0.08	0.04-0.11	0.06-0.10	0.045-0.09
III Dumb-bell, late stage	18-73	12-42	10-25	7-17	0.07-0.28	0.08-0.28	0.11-0.28	0.10-0.24	0.09-0.27
IV Egg shape	73-176	42-101	25-60	17-20	0.28-0.67	0.28-0.67	0.28-0.67	0.24-0.28	0.27-0.57
V Spherical	176-264	101-151	60-90	20-71	0.67-1.00	0.67-1.00	0.67-1.00	0.28-1.00	0.57-1.00
No rods evident	18-21	12-17	7-10	12-17	0.07-0.08	0.08-0.11	0.08-0.11	0.17-0.24	0.14
No dumb-bells evident	73-88	42-50	25-30	20-41	0.28-0.33	0.28-0.33	0.28-0.33	0.28-0.58	0.39

List of Figure captions

Figure 1 Spheronisation mechanisms according to (*a*) Rowe (1985); (*b*) Baert and Remon (1993); (*c*) combined deformation and agglomeration mechanism (Liew *et al*., 2007; Koester *et al*., 2012).

Figure 2 Photograph (plan view) of spheroniser plate in motion. The pellets move randomly in a 'rope' in the region near the wall.

Figure 3 Construction lines used in *AF* and *SF* calculation for one quarter of an arbitrary pellet with a confining circle of 8 equal segments (n = 8, ϕ = 45º). OAB is segment i, OBC segment i+1. Dot-dashed lines are chords constructed for the confining circle: angle α_i is the difference between the line with gradient of AB shifted to D (on pellet) and the corresponding pellet chord DE. β_i is angle DEF.

Figure 4 Effect of spheroniser rotational speed on end time, t_{end}. Experimental conditions: 21 °C, relative humidity 50%. Dashed locus shows line of best fit to the experimental data, equation [5]. Solid locus shows the simple model (Equation [A.3]) behaviour, $t_{end} \propto \omega^{-3}$, fitted through the datum at 1580 rpm. Error bars represent the uncertainty in end time estimation.

Figure 5 Photographs of pellets obtained from spheronisation of 2 cm rods at 1200 rpm for different times: t_{end} = 264 s. Fines removed for clarity.

Figure 6 Amount of material lost during spheronisation, either as fines or on machine. Error bars plotted for ω = 1200 rpm tests.

Figure 7 Evolution of (*a*) number of pellets (open symbols) and pellet length (solid symbols, plotted as average ± range), and (*b*) aspect ratio at different spheronisation times. Log scale used to show behaviour at small times. Initial values: N_p = 20, l = 20 mm, AR = 0.15. Labels I-V denote the stages of pellet shape evolution in Table 1. Error bars in (*b*) indicate the range of AR values measured.

Figure 8 Histograms showing evolution of (*a)* aspect ratio and (*b*) circularity at 1200 rpm.

Figure 9 Evolution of pellet shape, ω =1200 rpm. Each datum represents an individual pellet. Solid line shows geometric result for rods generated by rod breakup (Equation [8]). Dashed lines indicate approximate boundaries between shape stages in Table 1.

Figure 10 (*a*) Angularity and (*b*) shape factors for pellets spheronised at different speeds. Data sets are plotted as arithmetic mean ± range.

Figure 11 X-ray microtomography images of (*a*) extrudate and (*b*)-(e) pellets at different stages of spheronisation: (*b*) rounded rod; (*c*) dumb-bell early stage; (*d*) dumb-bell late stage; (*e*) spheroidal pellet. Light grey region is MCC material, darker grey background. Regions highlighted in (*c*)-(*e*) exhibit higher porosity.

Figure 12 Proposed phenomenological model for spheronisation of MCC paste extrudates

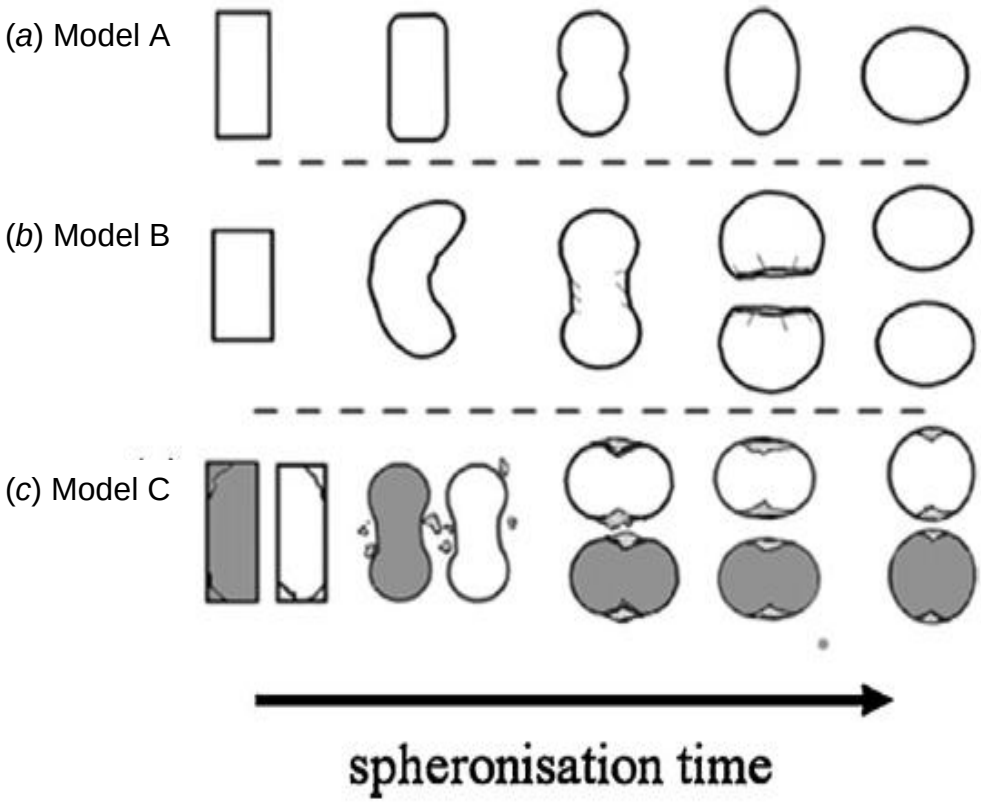

Figure 1 Spheronisation mechanisms according to (*a*) Rowe (1985); (*b*) Baert and Remon (1993); (*c*) combined deformation and agglomeration mechanism (Liew *et al*., 2007; Koester *et al*., 2012).

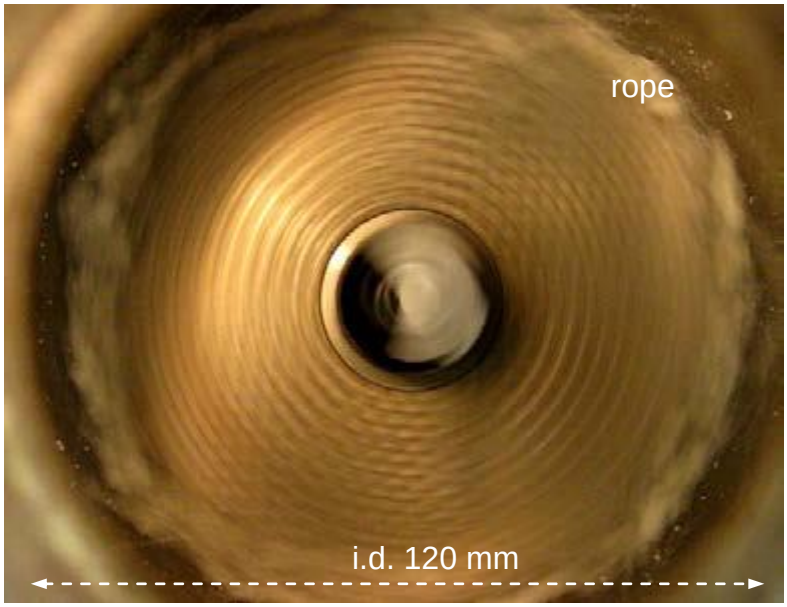

Figure 2 Photograph (plan view) of spheroniser plate in motion. The pellets move randomly in a ‘rope’ in the region near the wall.

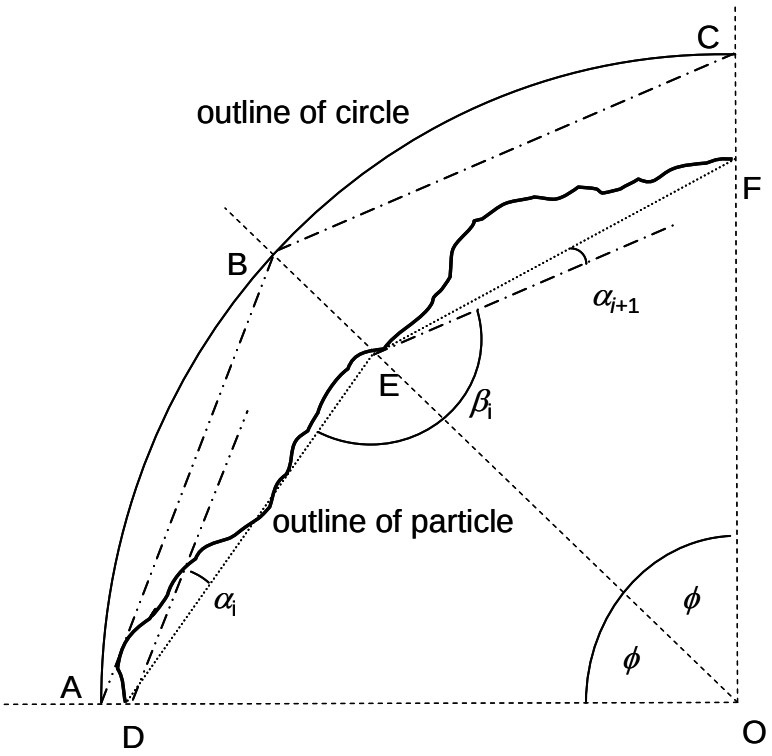

Figure 3 Construction lines used in *AF* and *SF* calculation for one quarter of an arbitrary pellet with a confining circle of 8 equal segments (n = 8, ϕ = 45º). OAB is segment i, OBC segment i+1. Dot-dashed lines are chords constructed for the confining circle: angle α_i is the difference between the line with gradient of AB shifted to D (on pellet) and the corresponding pellet chord DE. β_i is angle DEF.

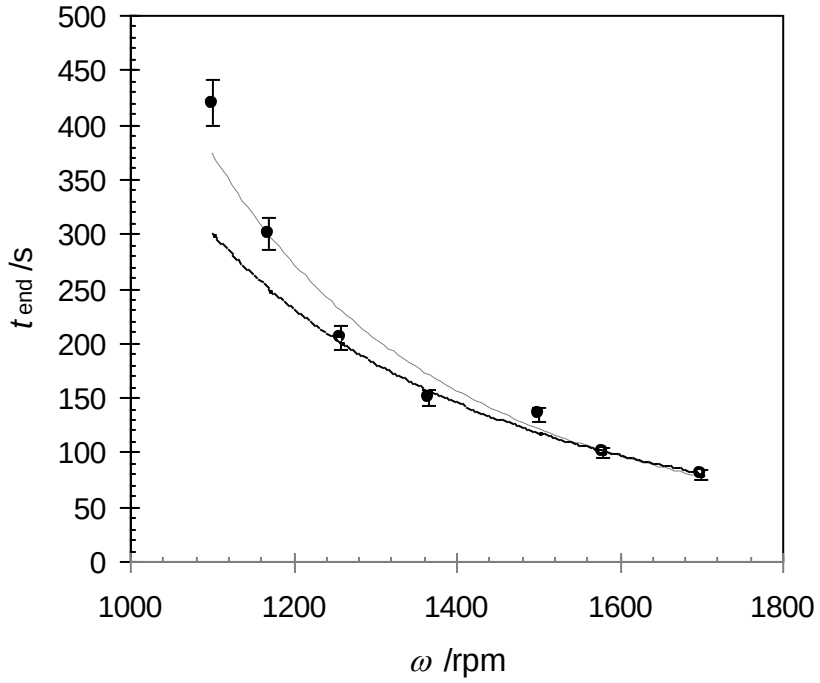

Figure 4 Effect of spheroniser rotational speed on end time, t_{end}. Experimental conditions: 21 °C, relative humidity 50%. Dashed locus shows line of best fit to the experimental data, equation [5]. Solid locus shows the simple model (Equation [A.3]) behaviour, $t_{end} \propto \omega^{-3}$, fitted through the datum at 1580 rpm. Error bars represent the uncertainty in end time estimation.

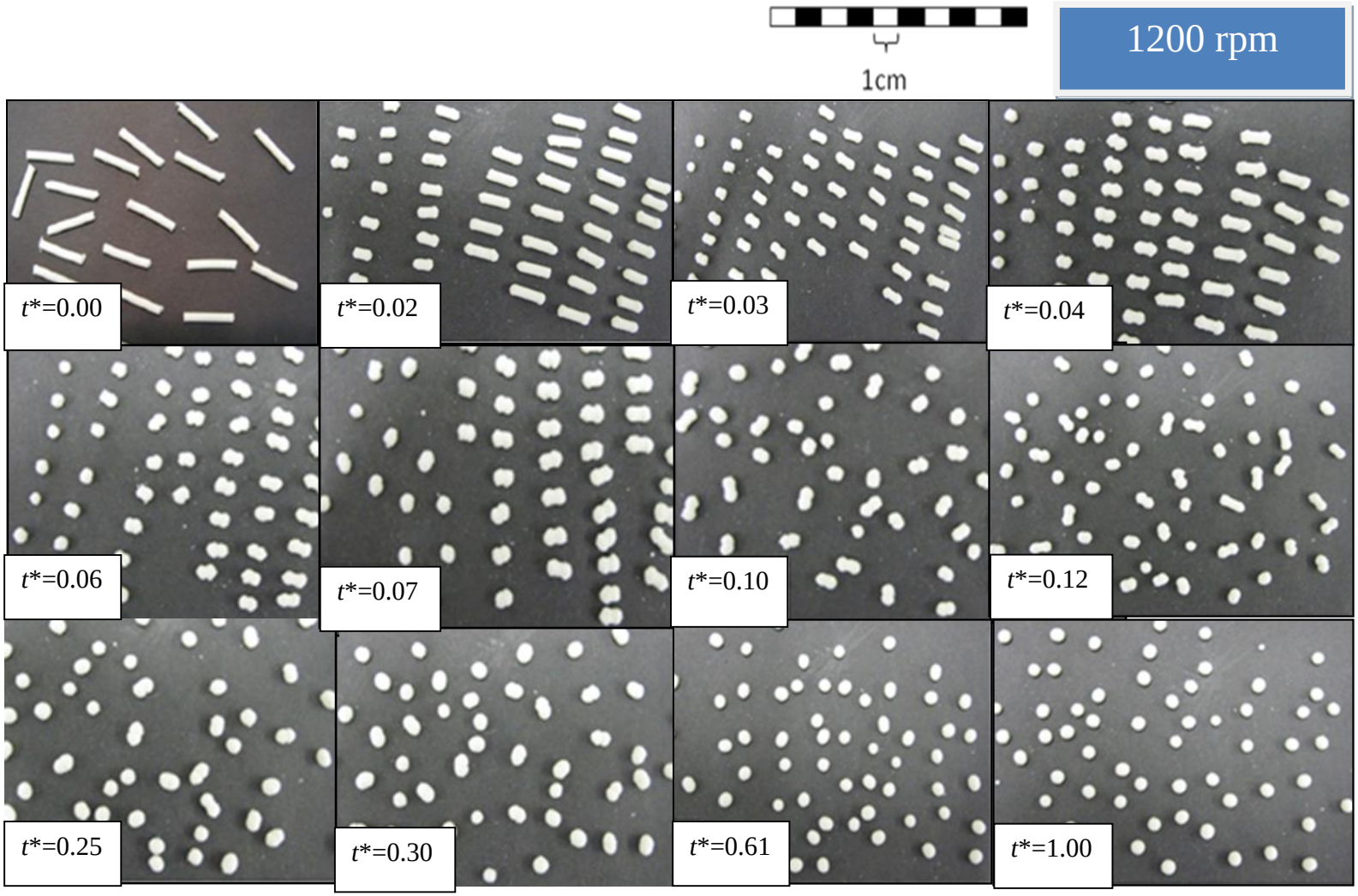

Figure 5 Photographs of pellets obtained from spheronisation of 2 cm rods at 1200 rpm for different times: t_{end} = 264 s. Fines removed for clarity.

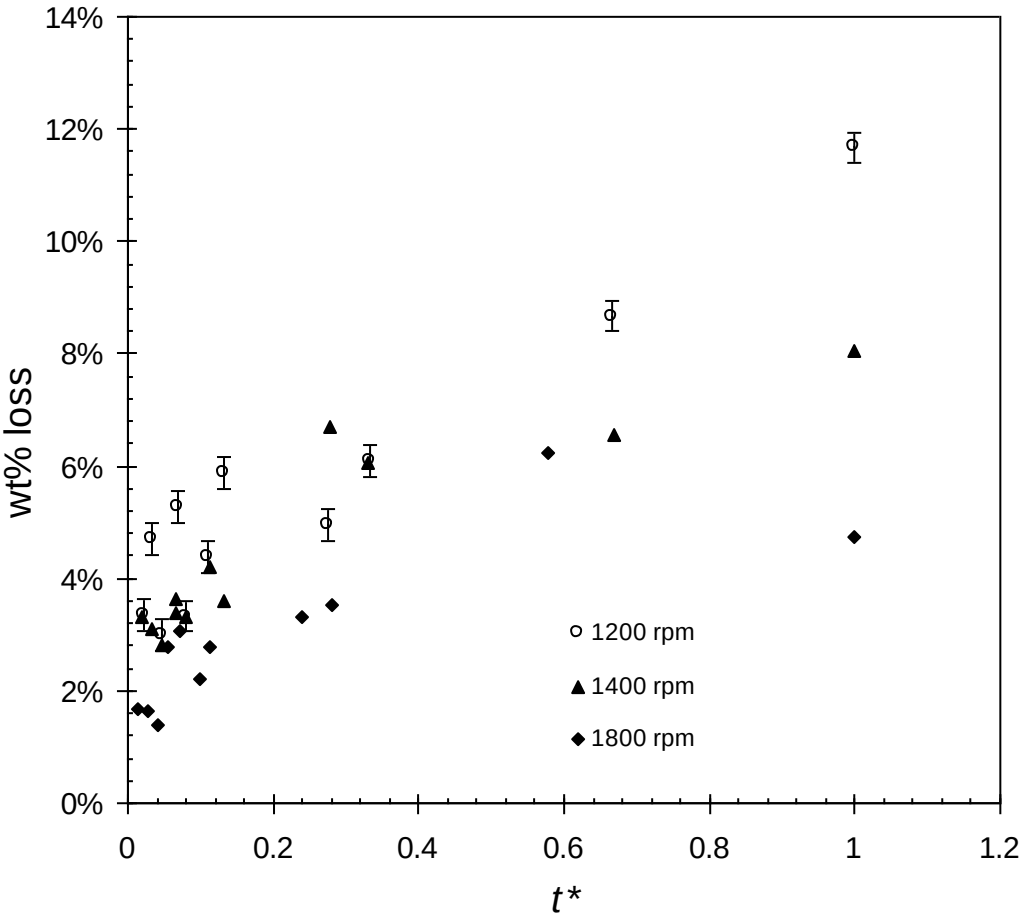

Figure 6 Amount of material lost during spheronisation, either as fines or on machine. Error bars plotted for ω = 1200 rpm tests.

(*a*)

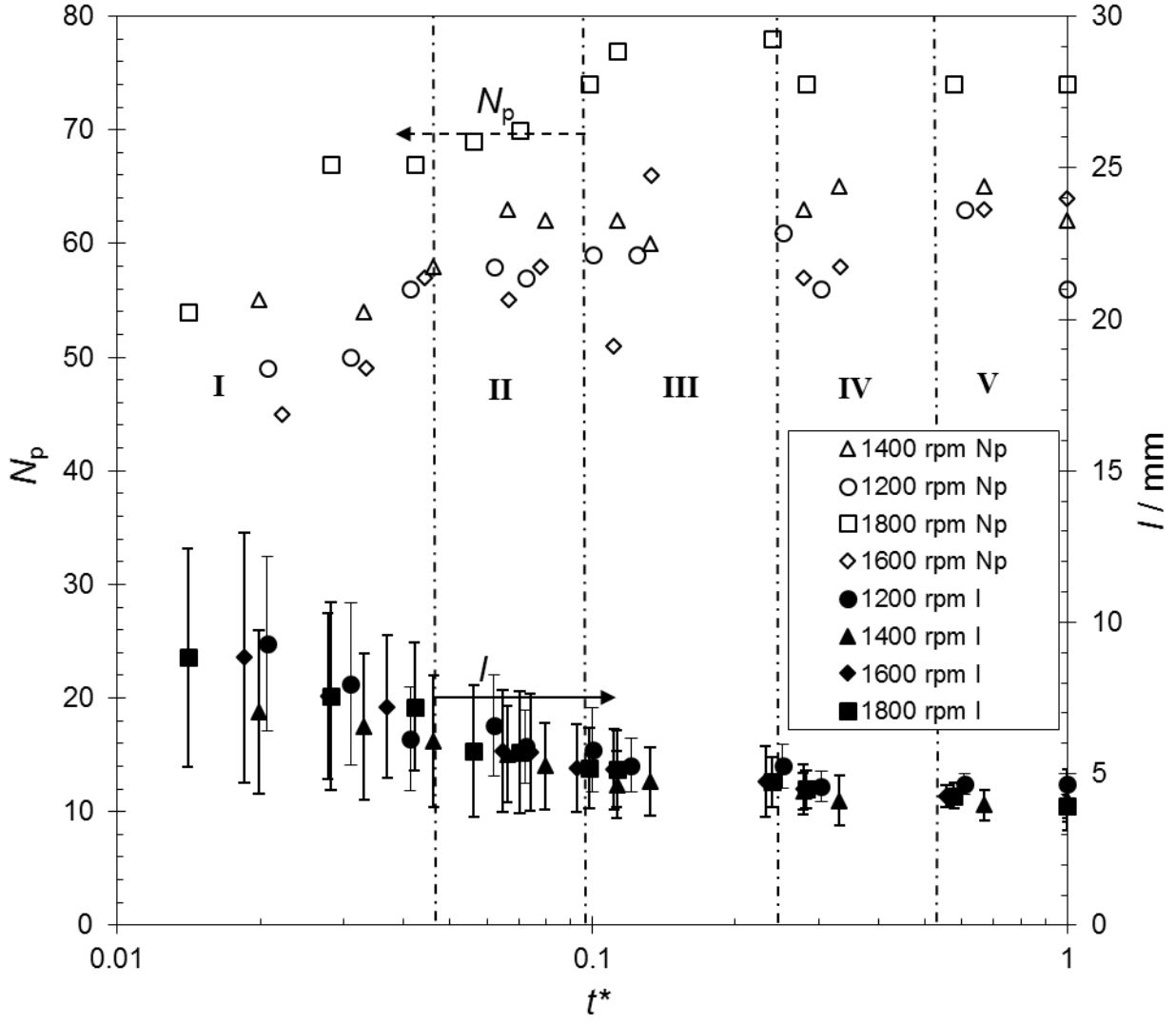

Figure 7 Evolution of (*a*) number of pellets (open symbols) and pellet length (solid symbols, plotted as average ± range), and (*b*) aspect ratio at different spheronisation times. Log scale used to show behaviour at small times. Initial values: N_p = 20, l = 20 mm, AR = 0.15. Labels I-V denote the stages of pellet shape evolution in Table 1. Error bars in (*b*) indicate the range of AR values measured.

(*b*)

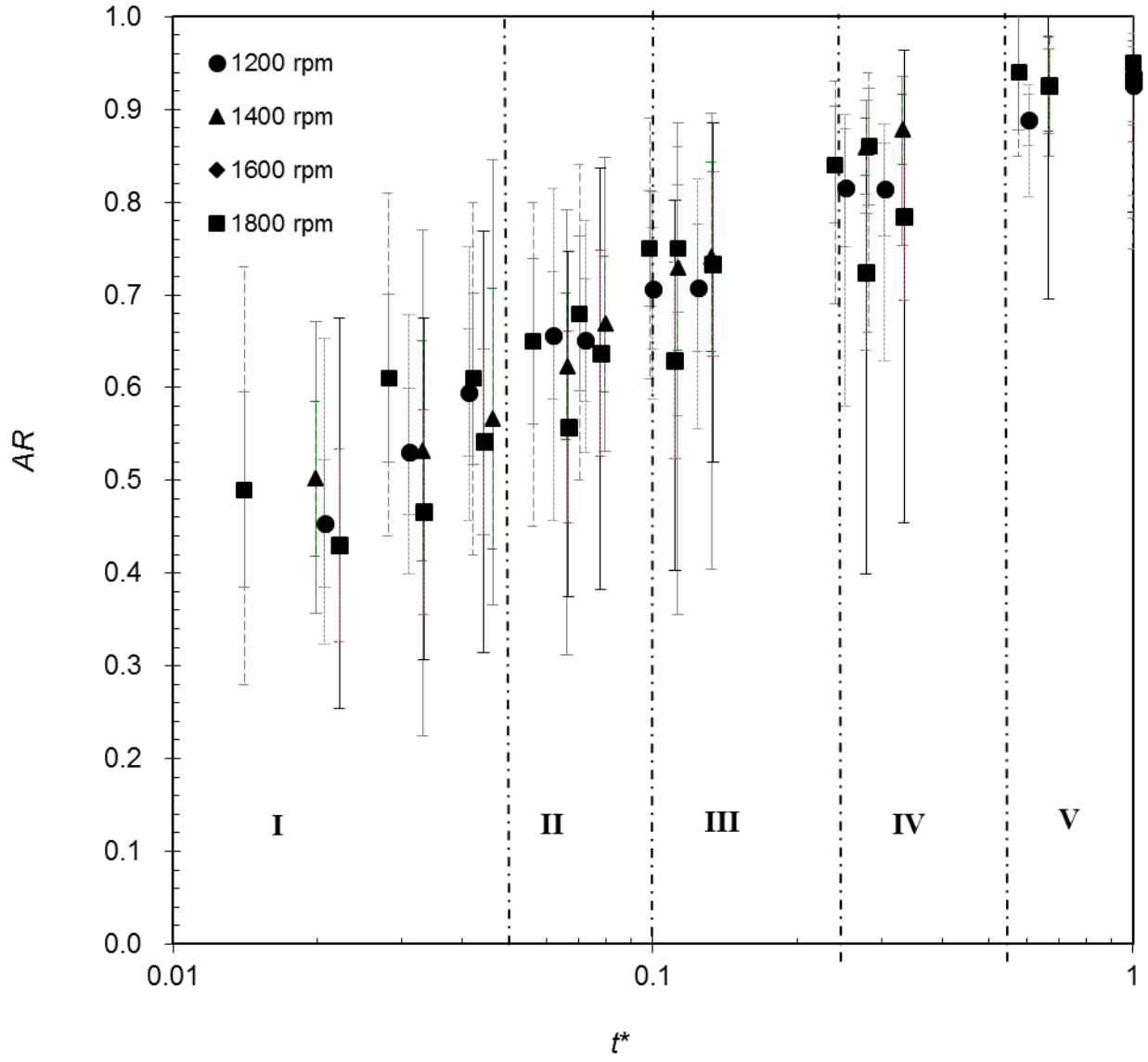

Figure 7 Evolution of (*a*) number of pellets (open symbols) and pellet length (solid symbols, plotted as average ± range), and (*b*) aspect ratio at different spheronisation times. Log scale used to show behaviour at small times. Initial values: N_p = 20, l = 20 mm, AR = 0.15. Labels I-V denote the stages of pellet shape evolution in Table 1. Error bars in (*b*) indicate the range of AR values measured.

(*a*)

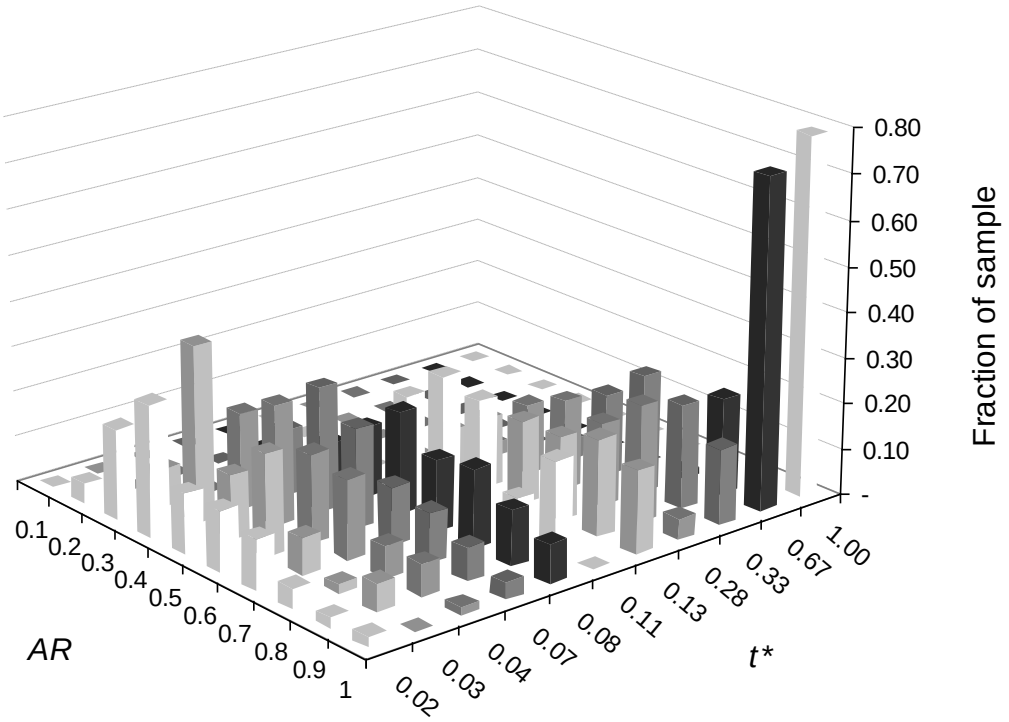

(*b*)

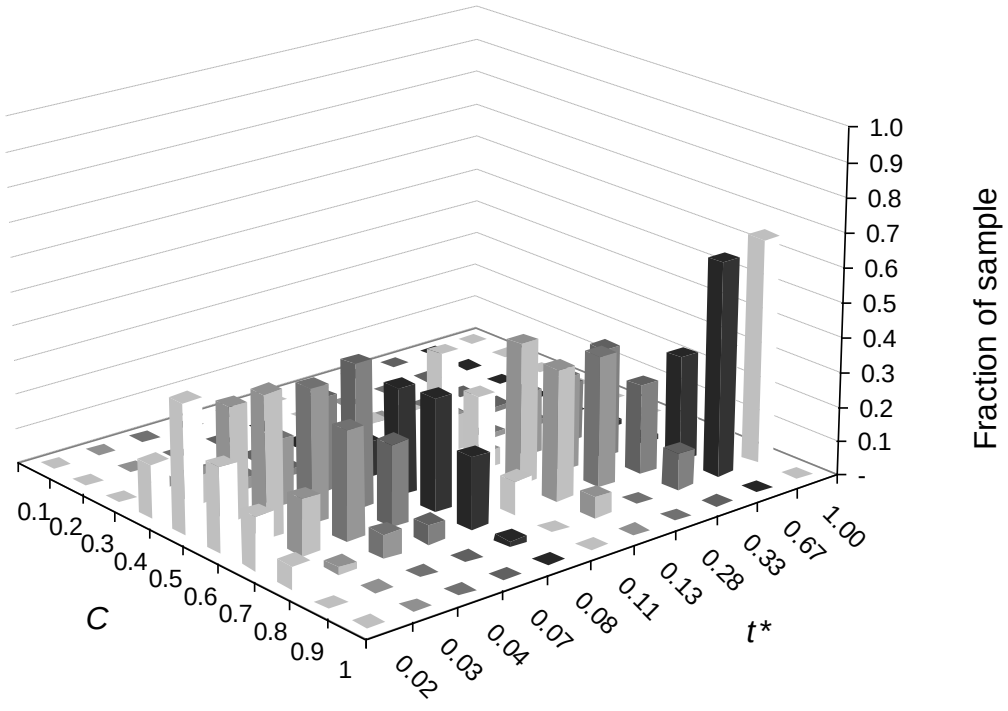

Figure 8 Histograms showing evolution of (*a)* aspect ratio and (*b*) circularity at 1200 rpm.

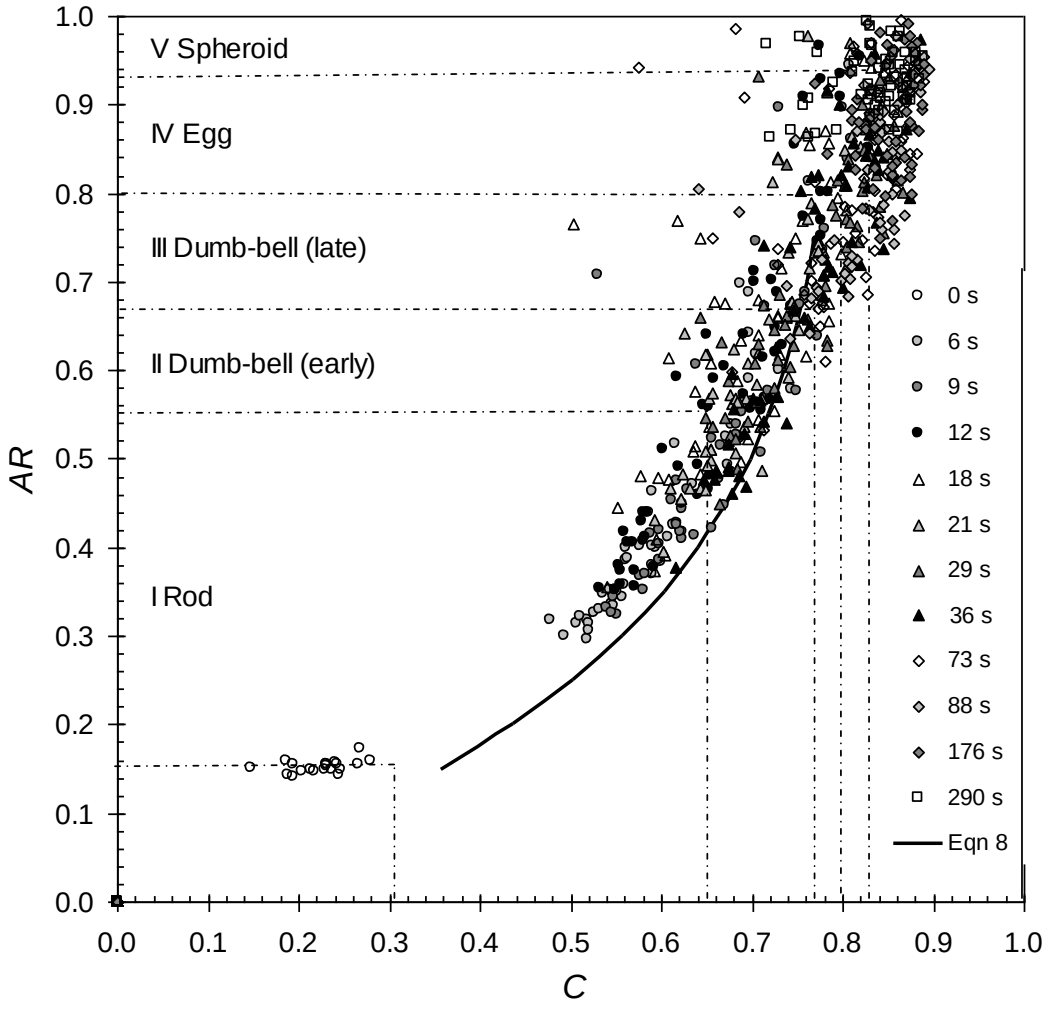

Figure 9 Evolution of pellet shape, ω =1200 rpm. Each datum represents an individual pellet. Solid line shows geometric result for rods generated by rod breakup (Equation [8]). Dashed lines indicate approximate boundaries between shape stages in Table 1.

(*a*)

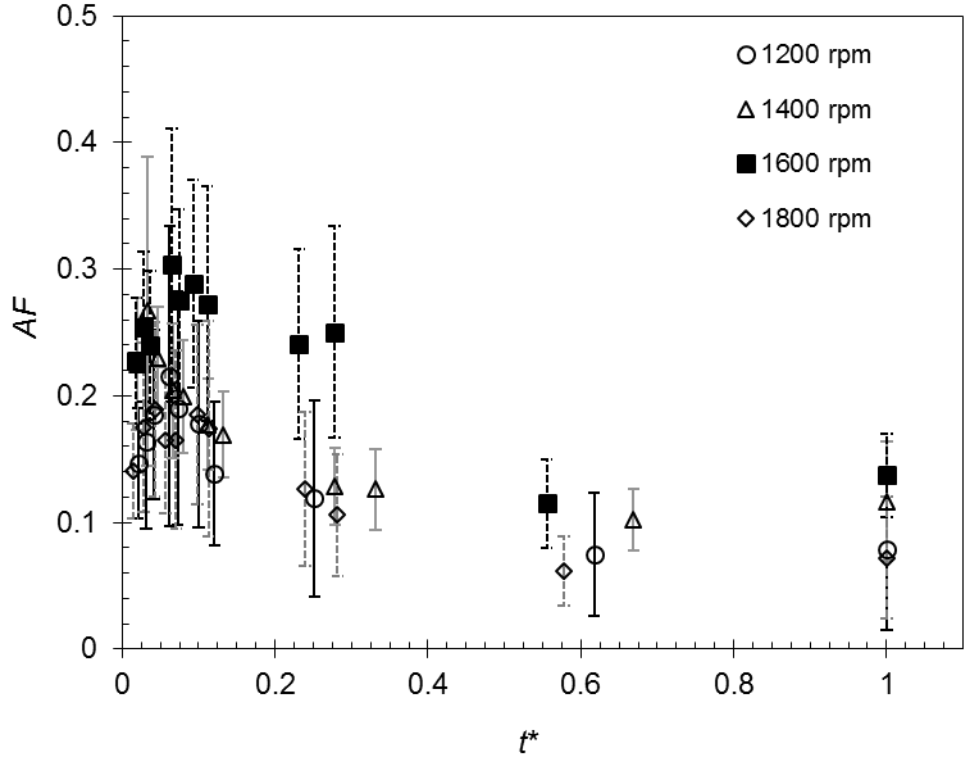

(*b*)

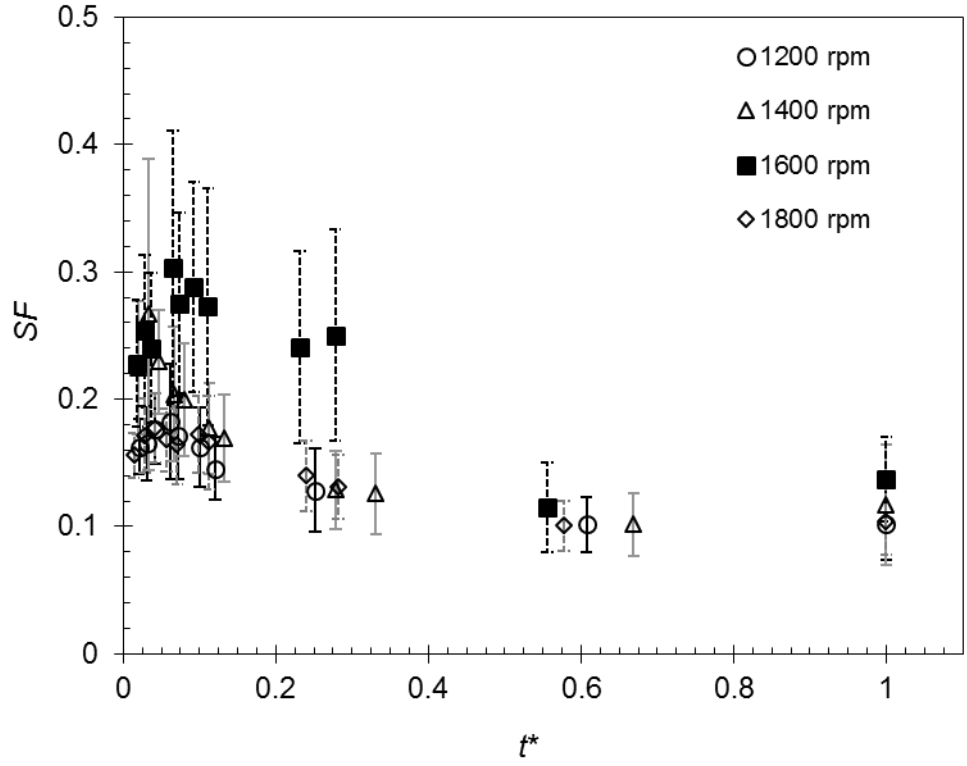

Figure 10 (*a*) Angularity and (*b*) shape factors for pellets spheronised at different speeds. Data sets are plotted as arithmetic mean ± range.

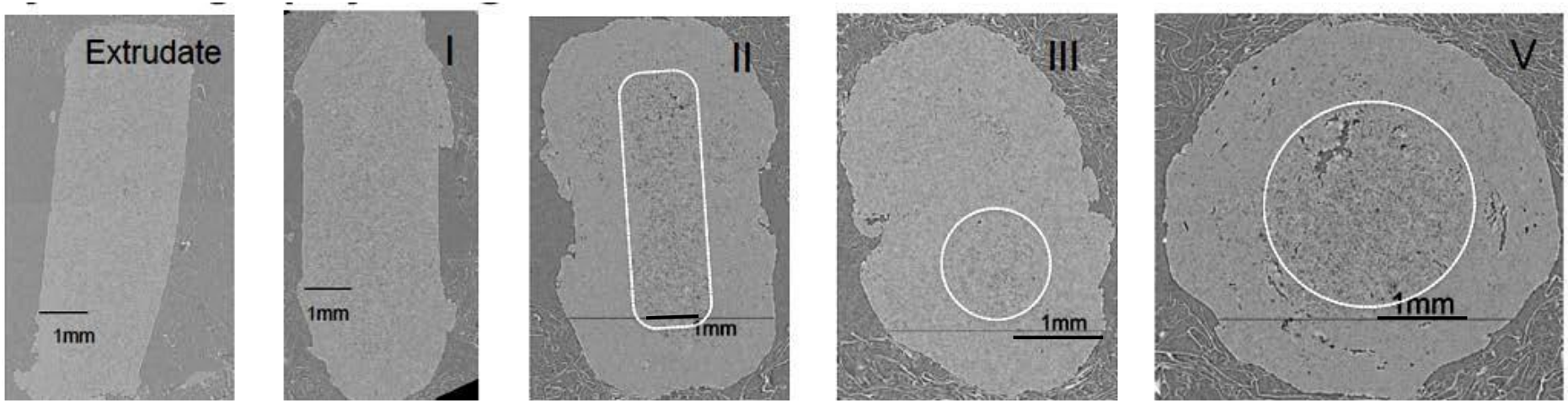

Figure 11 X-ray microtomography images of (*a*) extrudate and (*b*)-(e) pellets at different stages of spheronisation: (*b*) rounded rod; (*c*) dumb-bell early stage; (*d*) dumb-bell late stage; (*e*) spheroidal pellet. Light grey region is MCC material, darker grey background. Regions highlighted in (*c*)-(*e*) exhibit higher porosity.

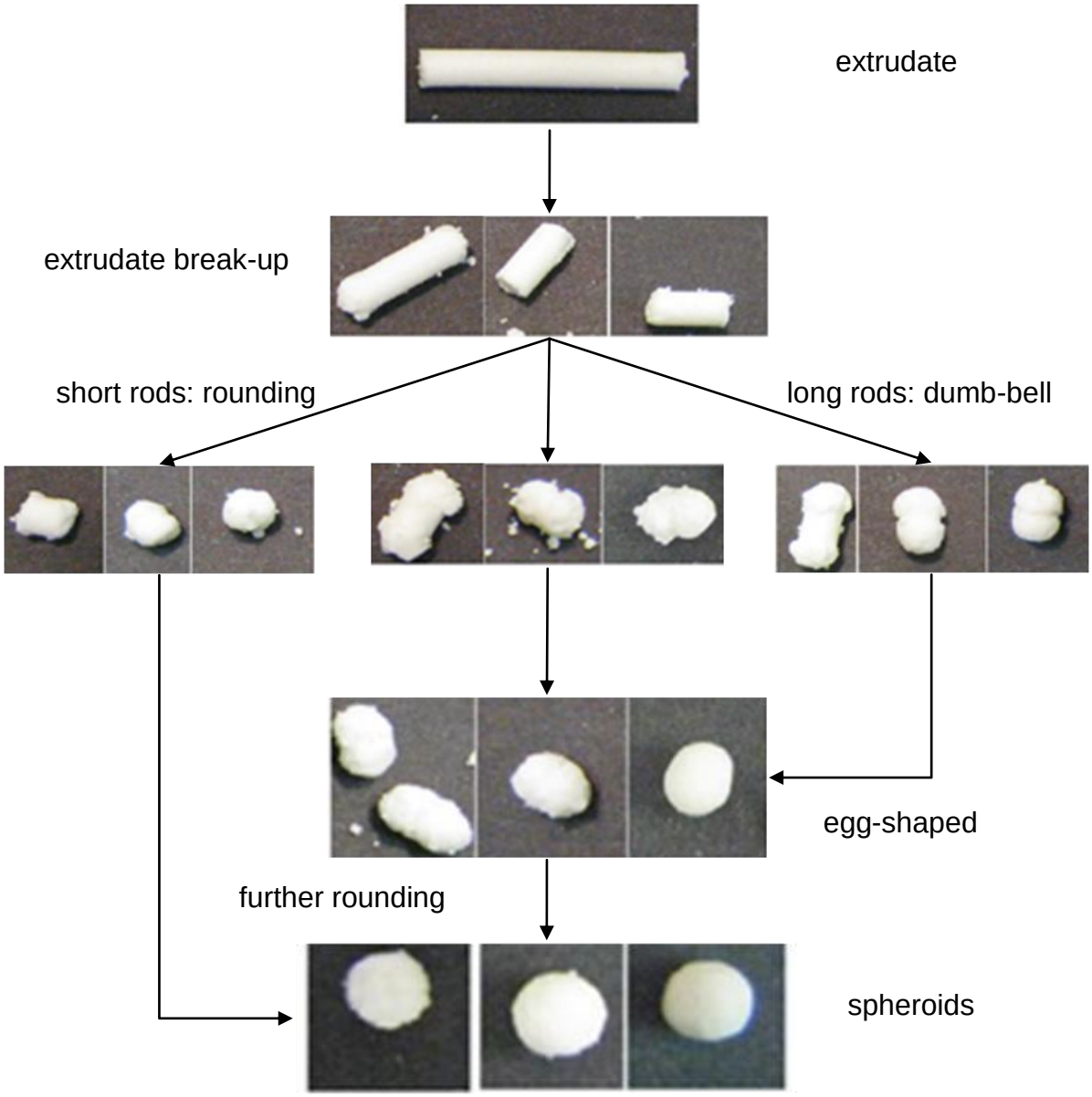

Figure 12 Proposed phenomenological model for spheronisation of MCC paste extrudates